Surface folding of viscoelastic fluids: finite elasticity membrane model

T. PODGORSKI† and A. BELMONTE

The W. G. Pritchard Laboratories, Department of Mathematics,
Pennsylvania State University, University Park, PA 16802, USA
email: `thomas.podgorski@ujf-grenoble.fr`, `belmonte@math.psu.edu`

When a dry sphere sinks into a fluid, a funnel-shaped free surface develops behind the sphere if the sinking occurs faster than the surface wetting. If the fluid is viscoelastic, the interface can become unstable to a loss of axisymmetry. The stress near this surface concentrates into boundary layers, as also seen in other free surface extensional flows of viscoelastic fluids. At high Deborah number and low Reynolds number, the qualitative behaviour can be recovered by considering the static equilibrium of a stretched elastic membrane in an hydrostatic pressure field. We treat this problem in the framework of finite elasticity using a neo-Hookean constitutive model, and show how the conditions of instability can be recovered. A numerical study of this model is presented.

1 Introduction

The axisymmetric shape known as a catenoid, which a soap film assumes when stretched between two rigid rings, is a classic example of a fluid surface shape determined by a force balance condition [3]; it also leads to a partial differential equation, the zero curvature equation (or minimal surface equation in integral form) [5, 10]. More generally, the forces which determine the shape of a fluid interface or a membrane bounding a fluid include the stresses in the fluid and the interfacial or membrane forces [17]. Examples of such shapes in nature include static [28] or dynamic [4] liquid menisci [6], viscous drops [25] or rivulets running down a plane [7], blood cells [8] and microscopic vesicles pulled by various manipulative forces or under flow [22]. While macromolecular fluids such as polymer solutions can have very different flow behavior than fluids which obey the Navier–Stokes equation [2], such differences are strikingly revealed in the presence of free surfaces. In a previous work we presented the observation of a new instability during the deformation of the free surface when a sphere sinks into a highly elastic fluid [18].

Consider a solid dry sphere dropped through the free surface of a viscous liquid, a polymer solution, or other complex fluid. In this situation there will be two competing effects: the wetting of the sphere's surface, and the stretching of the interface by the moving sphere. If the wetting velocity is small compared to the sinking velocity, a funnel shaped

---

† Present address: Laboratoire de Spectrométrie Physique, CNRS – Université Joseph Fourier (Grenoble I), France.
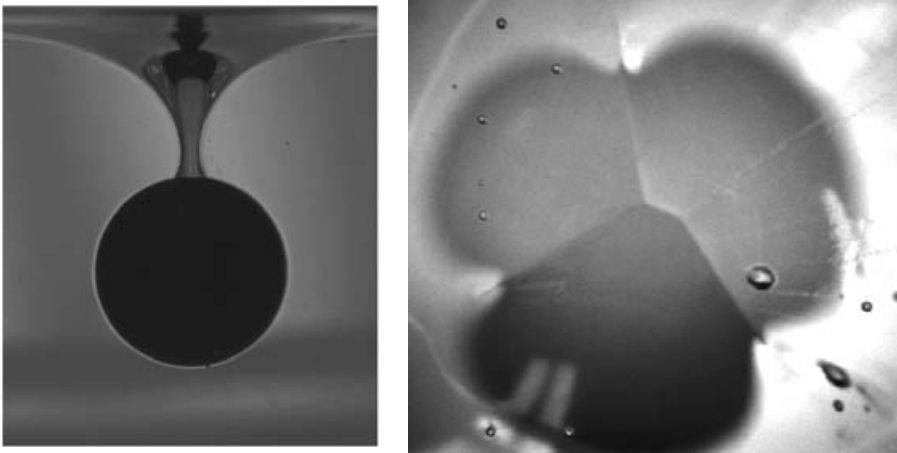
FIGURE 1. Elastic surface folds in aqueous solutions of 100 mM CPCl/60 mM NaSal: a) side view of a $1/2''$ diameter falling glass sphere; b) surface folds after pinch-off for a $3/4''$ teflon sphere (distorted image of sphere is visible below surface).

region is drawn out in the wake of the sphere, as seen in Figure 1a. In a viscoelastic fluid, this stretched surface becomes unstable and loses its original axial symmetry, an instability not observed in viscous Newtonian fluids [18]. Long after the sphere has detached from the surface and reached the bottom, folds are seen on the surface (Figure 1b).

Similar interfacial instabilities have actually been reported in various experiments involving viscoelastic fluids: air bubbles rising in a polymer solution exhibit a cusp at the trailing edge which is not axisymmetric [16], and radial fingering instabilities are observed when a filament of a viscoelastic fluid is stretched between separating plates [24]. Numerical studies of the latter phenomenon [19, 27] have shown that stress boundary layers develop near the free surface of the filament where the stress is an order of magnitude higher than in the bulk. Stress boundary layers have also been shown mathematically to occur near walls for the upper convected Maxwell model [21]; they have also been observed numerically downstream of stagnations points in flow past rigid or liquid spheres [12, 13]. Based on numerical observations, Arun Kumar & Graham [1] suggested that the radial fingering instability of stretched filaments could be at least qualitatively recovered by a simplified membrane model, in which the free surface is modeled by a purely elastic membrane and body forces are neglected.

Using a birefringence technique for stress visualization, we showed that stress boundary layers were also forming in our experiment [18]. This suggested that the interface shapes were primarily the result of a quasi-static equilibrium of elastic forces concentrated in a thin boundary layer and hydrostatic pressure in the fluid. We also showed that under certain conditions, an elastic membrane model would lead to a buckling instability which resembled our experimental observations [18]. This instability requires that the azimuthal component of the elastic tension T_2 become negative. To show that such negative stresses can actually develop in the context of finite elasticity theory, we present here a study of a specific elastic constitutive equation, which we solve numerically to get axisymmetric solutions of the interface shape and the associated distribution of stresses.

The general form of the equation for quasi-static equilibrium is a simple force balance:

$$T_1\kappa_1 + T_2\kappa_2 = P \tag{1.1}$$

where the subscripts 1 and 2 denote the directions of principal curvature of the surface, κ_i and T_i the corresponding curvatures and tensions, and P the internal (hydrostatic) pressure. Thus, the problem can be viewed as a generalization of the classical minimal surface problem where $\kappa = \kappa_1 + \kappa_2 = 0$, with a non-uniform pressure P on the surface and a non-isotropic and non-uniform tension T. It is relevant to any physical situation where anisotropy of surface tension can appear and influence the interface shape: non-Newtonian fluids, elastic membranes or liquid crystals.

2 Experimental results

Our experimental exploration of this phenomenon was conducted with a simple setup: a dry rigid sphere was gently released at the surface of a viscoelastic fluid in a rectangular plexiglas container (length 15 cm, width 6 cm, height 10 cm). To define the initial conditions reproducibly, the sphere was held half-immersed in the fluid with tweezers, and released at rest. As the sphere began to sink into the fluid, it deformed the interface.

The fluid itself was an aqueous solution of a surfactant, cetylpyridinium chloride (CPCl), and an organic salt, sodium salicylate (NaSal), with respective molar concentrations of 100 mM and 60 mM; this system forms long wormlike micelles, and its viscoelastic properties are well known [20, 23]. More details of the experimental setup can also be found in Podgorski & Belmonte [18].

If the wetting velocity of the interface along the surface of the sphere U_s is small compared to the sinking velocity through the bulk U_b, which happens when the sphere is made of a poorly wettable material such as Teflon, the interface is stretched into a funnel shape sketched in Figure 2. When the liquid is a very viscous Newtonian fluid, the interface is axisymmetric, as seen from above in Figure 3a. This interface continues to close up symmetrically, and eventually pinches off at a point (final frame of Figure 3a). While the actual shape of this interface in the viscous case poses an interesting mathematical question itself, our primary concern here is with what changes when the fluid has an additional elasticity.

In the non-Newtonian case, a similar funnel shape occurs, but becomes unstable to a loss of axisymmetry (3b). This perturbation ultimately results in the interface pinching off along a *line* [18]. The instability also leads to long-lived surface folds, like the one seen in Figure 1b and the last frame of Figure (3b), which are creases in the fluid surface often taking several minutes to completely relax. The most spectacular observations of this phenomenon were made using viscoelastic micellar fluids [18], but it was observed in several polymer solutions as well.

A remarkable feature of the flow is the formation of stress boundary layers at the free surface: taking advantage of the birefringence properties of the fluid to visualize the stress, we showed in a previous paper that the stress is concentrated near the fluid interface [18], while flow visualization indicates an associated strong stretching flow near the interface and much smaller velocities in the bulk.
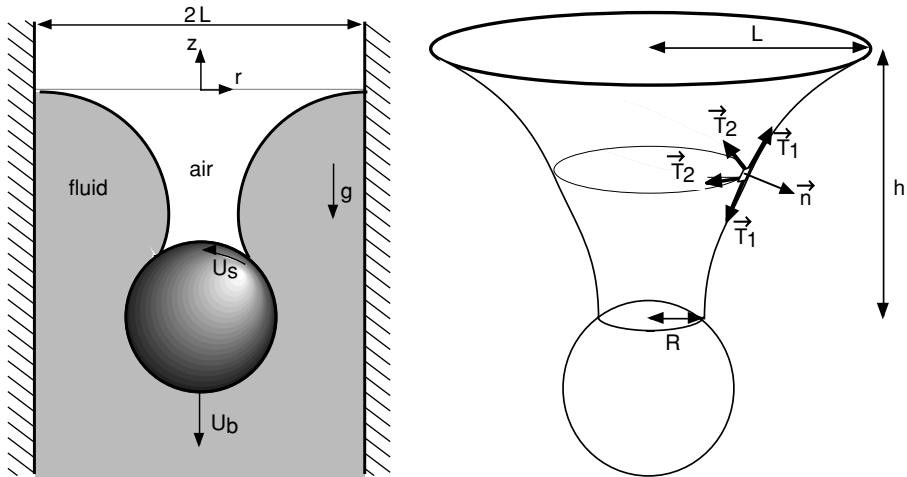
FIGURE 2. Deformation of the interface when a sphere sinks through a fluid, and notation for the model. The axisymmetric surface has a radius L at the top, and stretches to a depth h where it has radius R.
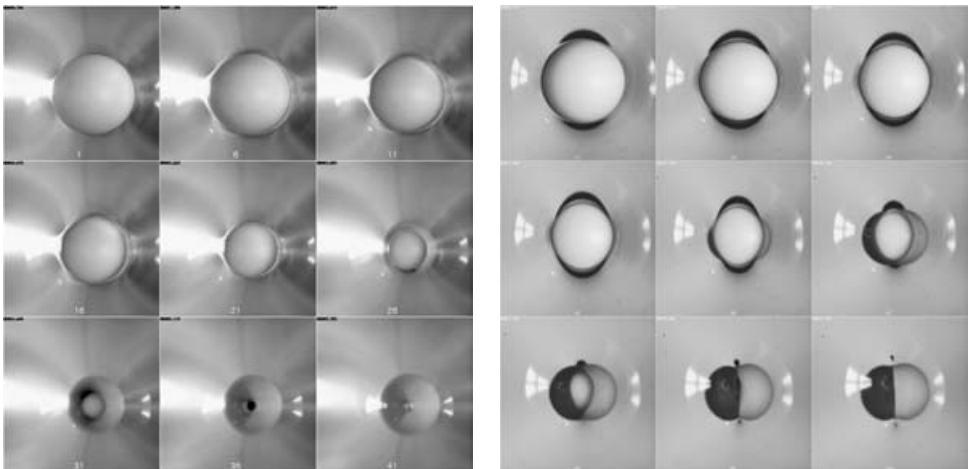

FIGURE 3. Top view of a 3/4″ teflon sphere falling into: a) 30,000 cSt silicone oil (Newtonian) $\Delta t = 0.625$ s; b) 100 mM CPCl/60 mM NaSal (non-Newtonian) $\Delta t = 2.75$ s.

A streak image of the flow field around a 3/4″ Teflon sphere sinking in a solution of 100 mM CPCl/60 mM NaSal is shown in Figure (4); the streak lines are much longer near the surface, revealing the strong stretching flow there. We concluded that on the time scale of the phenomenon, elastic stresses – concentrated near the stretched interface – are dominant over viscous forces, and that the slow bulk flow does not contribute much to the force balance governing the shape of the interface. This motivated us to formulate a simple model for the viscoelastic interface.
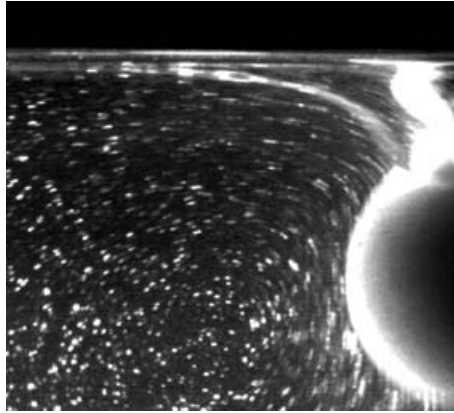
FIGURE 4. Streak visualization of the flow field around a 3/4″ Teflon sphere sinking in 100 mM CPCl/60 mM NaSal solution. The particles paths shown correspond to $\Delta t = 1.67$ s.

3 Mathematical models for the viscoelastic free surface

To summarize our experimental observations, the flow which gives rise to the folding of the viscoelastic interface has the following characteristics:

- the flow speed is very weak far from the interface, and the Reynolds number is small (typically 10^{-3});
- elastic effects are large, and thus the Deborah number $De \sim 1$ [2], while the extension ratios are relatively high near the interface where they form a thin stress boundary layer.

These observations motivated us to construct a simple model which approximates the experimental situation in terms of a simplified picture, in an attempt to capture the essential elements of this instability.

We divide the fluid into two regions: a 'membrane' representing the interfacial stress boundary layer, which we suppose to be purely elastic, and a static fluid reservoir. In this approximation, we neglect the relaxation effects of the fluid during the time of the experiment, and all other flow effects in the bulk. The shape of the interface in our model is determined only by the elastic forces of the thin membrane stretched by the falling sphere, and the hydrostatic pressure in the surrounding fluid.

Since we do not actually solve for any flow field, we do not treat the formation or subsequent evolution of the stress boundary layer. We note the similarity of our approach with the simplified model of Harlen *et al.* [13] for non-Newtonian flow downstream of a stagnation point, which they called the *birefringent strand technique*. They took a boundary layer approach to the highly concentrated stress in the wake of a rigid sphere; this 'birefringent strand' was replaced in their model by a viscous Newtonian fluid of high viscosity, which was embedded in a less viscous Newtonian fluid. It was later found that the thickness of this strand can depend on the details of the flow [12]. In our situation the flow in the bulk is much weaker, and we retain only the hydrostatic pressure contribution, whereas the boundary layer region is completely elastic. Since we could not

experimentally determine any dynamics of the apparent thickness of the stress boundary layer with enough precision [18], we will assume for simplicity that the volume of the membrane in our model is constant in time, with an initial effective thickness w in the unstressed reference state. This is a strong and critical assumption for our model, which in the future should be replaced, once there is some indication as to how material joins or leaves the membrane.

3.1 General equations

The overall geometry of the problem, and the notation used in the model, are shown in Figure 2. The local equation of equilibrium for the membrane in a given shape is a balance between the normal resultant of surface forces and the pressure jump across the membrane [11]:

$$T_1 \kappa_1 + T_2 \kappa_2 = -\rho g z, \tag{3.1}$$

where T_1 and T_2 are the tensions in the directions of principal curvature (meridional and azimuthal in the axisymmetric case), and κ_1 and κ_2 are the corresponding curvatures. The term on the right is the hydrostatic pressure of the fluid, where ρ is the density and g the acceleration of gravity.

In most practical cases and for axially symmetric problems, the profile of the membrane can be described by a function $r(z)$ relating the vertical coordinate z to the radius r. The force balance can be rewritten in the following form:

$$T_1 \frac{r''}{(1 + (r')^2)^{3/2}} - T_2 \frac{1}{r(1 + (r')^2)^{1/2}} + \rho g z = 0. \tag{3.2}$$

This equation is a generalization of more standard equilibrium equations for static interfaces which we shall briefly review before treating the elastic case.

For instance, if $\rho = 0$ and $T_1 = T_2 = \sigma$, where σ is the (constant) surface tension, one obtains the axisymmetric zero curvature equation $\kappa_1 + \kappa_2 = 0$ or $rr'' - r'^2 = 1$, which can also be derived from a minimal surface condition in variational form [5, 10]. This equation governs for instance the shape of a soap film stretched between two circular rings. The solutions are catenoids of the form $r(z) = a \cosh(z/a)$ [3, 5] when the ratio of the axial separation of the rings h to their radius R is smaller than approximately 1.325 (the parameter a has two branches of solutions, one of which is unstable, corresponding to a maximal surface). When $h/R \gtrsim 1.325$, the connected solutions (catenoids) disappear and only the trivial solution remains (two planar soap films in the rings). Thus, a soap film held between two rings *has a finite extensibility and disconnects when stretched too far*.

With $\rho \neq 0$ and $T_1 = T_2 = \sigma$, the equation governs the equilibrium of a hole in a static Newtonian fluid pool, e.g. a circular hole in a liquid film on a horizontal surface, as studied by Taylor & Michael [26]. In this case, for a given contact angle θ between the solid surface and the liquid–air interface, there exists a unique unstable solution if the liquid film thickness h is smaller than a critical thickness $h_c = 2\sqrt{\sigma/(\rho g)} \sin(\theta/2)$. When $h > h_c$, there is no solution: for geometrical reasons, the curvature does not allow the capillary forces to balance the hydrostatic pressure.

More generally, $\rho \neq 0$ and the tension is anisotropic ($T_1 \neq T_2$), which is essentially an elastic membrane in a hydrostatic pressure field. One way to physically obtain such a situation is to stretch an initially isotropic membrane, which means that T_1 and T_2 will depend on the location in the membrane and the deformation relative to the unstretched reference state.

3.2 Constant anisotropic surface stresses

In our first study [18], we considered T_1 and T_2 as constants, ignoring the fact that they are actually scalar functions determined by the total deformation. Our experiment has shown that the instability grows near the waist, where T_1 and T_2 presumably reach an extremal value because the deformation is maximal there. As a consequence, we assumed that there is a region in the neighborhood of the waist where T_1 and T_2 can be considered constant. In this section, we summarize the calculation developed in the previous paper [18], valid only near the waist located at $z = h_w$.

One can define a characteristic length scale for the problem:

$$\ell = (T_1/\rho g)^{1/2}. \tag{3.3}$$

This length sets the order of magnitude of the meridional curvature κ_1, and is similar to the capillary length $(\sigma/\rho g)^{1/2}$ appearing in Newtonian interfacial phenomena. By restricting our analysis to the neighborhood of the waist, where $r'(z) \ll 1$, and by nondimensionalizing the lengths with the characteristic length scale ℓ, the equilibrium equation 3.2 reduces to:

$$r''(z) - \beta r^{-1} + z = 0 \tag{3.4}$$

where $\beta = T_2/T_1$.

The results of our previous study of this equation showed that the solution is stable to azimuthal perturbations near the waist $z = h_w$ unless $\beta < 0$ [18]. Thus in the Newtonian case for which $\beta = 1$ (Figure 3a), the axisymmetric solution is stable. In the non-Newtonian case, for which β is not determined, the folding instability (Figure 3b) indicates that β must be negative. Thus either T_2 or T_1 must become negative (compressive). We will address this possibility directly in this paper, and show that such a negative surface stress can physically occur in the context of our membrane model. A similar negative surface stress was seen in the dynamics of a stretched viscoelastic filament by Forest & Wang [9], which led to an ill-posedness in their numerical simulations.

3.3 Finite elasticity model

Here we study a specific elastic constitutive equation, which explicitly relates the tensions $T_1(z, t)$ and $T_2(z, t)$ to the surface distortion and shape. In contrast with the case of simple interfaces, where surface tension is a constant, in an elastic membrane the tensions T_1 and T_2 are functions of the position in the membrane and the local deformation. Thus they depend on the distortion and shape of the interface relative to a stress-free reference state.
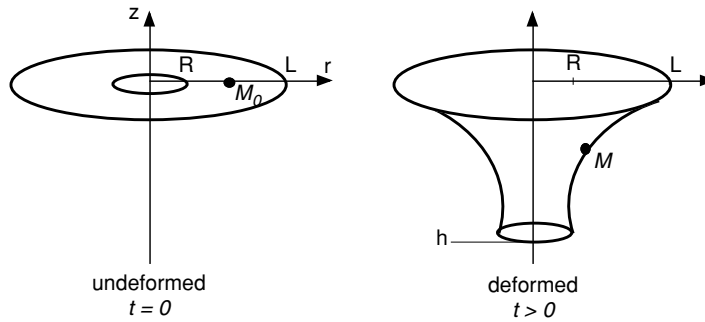
FIGURE 5. Setup for the finite elasticity model: the membrane is assumed to be fully relaxed in its initial configuration, a disk of exterior radius L, with a hole of radius R in the center. In the deformed state, the circle of radius R is pulled down to a depth h.

We consider the problem as shown in Figure 5, where an initially flat surface is pulled downward into a hydrostatic pressure field:

- at $t = 0$, the sphere is half-submerged in fully relaxed fluid (axisymmetric domain). The relaxed shape of the membrane is a disk of radius L with a circular central hole of radius R, where the outer boundary corresponds to the container wall (radius L) in the experiment, and R is the radius of the sphere.
- at time $t > 0$, the sphere has sunk, and all elements in the disk are mapped to the stretched surface ($M_0 \rightarrow M(t)$). The outer boundary remains at $z = 0$ with a radius L, and the inner boundary is drawn down to $z = h$. For simplicity, we assume the radius of this circle is constant and always equal to R, thereby neglecting the motion of the contact line on the sphere (the wetting velocity is supposed very small compared to the sinking velocity)

A material point on the membrane, such as M_0 shown in the figure, can be labelled by its radial coordinate p in the coordinates of the unstretched state. In the deformed state at time t, the corresponding point $M(t)$ is specified by two coordinates (r, z). The solution of the problem consists in determining the mapping $M_0(p, 0) \rightarrow M(r, z)$, or in other words the functions $r(p)$ and $z(p)$, along with the corresponding stress fields. In this formulation, p is the material coordinate.

We label the meridional direction (along streamlines) as index 1, the azimuthal direction as 2, and the direction normal to the membrane as 3 (in the direction of the thickness). Because the deformations of the relaxed flat surface into the funnel shape are large, one must use the equations of finite elasticity to calculate the tensions [11].

For an axisymmetric membrane, one can define the extension ratios in the principal directions λ_j as [11]:

$$\lambda_1 = \frac{ds}{dp} = \left(\left(\frac{dr}{dp} \right)^2 + \left(\frac{dz}{dp} \right)^2 \right)^{1/2} = \sqrt{r'^2 + z'^2} \qquad (3.5)$$

$$\lambda_2 = \frac{r}{p} \qquad (3.6)$$

$$\lambda_3 = \frac{1}{\lambda_1 \lambda_2}, \tag{3.7}$$

where s is the arclength along the meridian curves, and the third relation (incompressibility) comes directly from our assumption that the volume of the membrane does not change in time.

The surface stresses (tensions) are functions of the local extension ratios, which depend on the global deformation of the membrane. For axisymmetric problems, the relation between the meridional and azimuthal tensions and the local extension ratios are given by [11]:

$$T_1 = 4w\lambda_3 \left(\lambda_1^2 - \lambda_3^2\right) \left(\frac{\partial W}{\partial I_1} + \lambda_2^2 \frac{\partial W}{\partial I_2}\right) \tag{3.8}$$

$$T_2 = 4w\lambda_3 \left(\lambda_2^2 - \lambda_3^2\right) \left(\frac{\partial W}{\partial I_1} + \lambda_1^2 \frac{\partial W}{\partial I_2}\right) \tag{3.9}$$

where w is the membrane thickness at rest, W is the strain energy function which depends on the strain invariants $I_1 = \sum_i \lambda_i^2$ and $I_2 = \sum_i \lambda_i^{-2}$ through a constitutive equation. The simplest constitutive equation for elastic materials is the neo-Hookean model, which we will use here:

$$W = C(I_1 - 3), \tag{3.10}$$

where C is a constant. The tensions are then:

$$T_1 = 4Cw\lambda_3 \left(\lambda_1^2 - \lambda_3^2\right) \tag{3.11}$$

$$T_2 = 4Cw\lambda_3 \left(\lambda_2^2 - \lambda_3^2\right). \tag{3.12}$$

The full model consists of a normal force balance (3.1), rewritten as a function of $r(p)$ and $z(p)$ and an internal equilibrium condition (tangential force balance):

$$T_1 \frac{r''z' - r'z''}{(z'^2 + r'^2)^{3/2}} - T_2 \frac{1}{r(1 + r'^2/z'^2)^{1/2}} + \rho g z = 0 \tag{3.13}$$

$$\frac{d}{dp}(T_1 r) = T_2 \frac{dr}{dp} \tag{3.14}$$

plus the neo-Hookean constitutive equation. One can rescale all tensions with Cw, and all lengths with the characteristic length scale $\sqrt{Cw/(\rho g)}$ which plays a role similar to the capillary length in ordinary interfacial problems, to get a dimensionless system of equations:

$$\lambda_1 = \sqrt{r'^2 + z'^2} \tag{3.15}$$

$$\lambda_2 = \frac{r}{p} \tag{3.16}$$

$$\lambda_3 = \frac{1}{\lambda_1 \lambda_2} \tag{3.17}$$

$$T_1 = 4\lambda_3 \left(\lambda_1^2 - \lambda_3^2 \right) \tag{3.18}$$

$$T_2 = 4\lambda_3 \left(\lambda_2^2 - \lambda_3^2 \right) \tag{3.19}$$

$$T_1 \frac{r''z' - r'z''}{(z'^2 + r'^2)^{3/2}} - T_2 \frac{1}{r(1 + r'^2/z'^2)^{1/2}} + z = 0. \tag{3.20}$$

$$T_1'r + (T_1 - T_2)r' = 0 \tag{3.21}$$

We solve these equations numerically for $r(p)$, $z(p)$, $T_1(p)$, and $T_2(p)$ given values of R, L, and h, with the spatial boundary conditions (see Figure 2):

$$r(R) = R, \qquad r(L) = L, \qquad z(R) = h, \qquad z(L) = 0 \tag{3.22}$$

4 Numerical results

4.1 Method

The coupled second order nonlinear differential equations (3.15)–(3.21) together with the boundary conditions 3.22 form a nonlinear boundary value problem which we approach numerically. In some cases, namely when the deformations are small and evenly distributed along the membrane, a simple 'shooting method' can be used by specifying $r(R)$, $z(R)$ and a rough guess of $r'(R)$ and $z'(R)$. However, in the general case, the convergence becomes very sensitive to the guessed value of the derivatives at $p = R$ and usually does not converge. We therefore also employed an iterative relaxation method [15], which solves for successive approximations of the solution. The equations are linearized about a guessed solution and then solved. The procedure is then repeated using the previous solution as a new guess until sufficient accuracy is obtained. In many cases, simple polynomials satisfying the boundary conditions are good starting functions for $r(p)$ and $z(p)$. When convergence was more difficult to achieve, we used the solution obtained for slightly different boundary conditions – after adequately rescaling it – as a starting function.

This solution was computed with the software package MATHEMATICA 3.0, which provides built-in functions making this method very efficient. An example of our technique is shown in Figure 6, where good convergence is obtained after only 4 iterations, with straight lines as starting functions. This provides us with a very good approximation to the shape of the membrane $(r(p), z(p))$. Unless stated otherwise, the results presented hereafter are for a purely elastic membrane with $\sigma = 0$.

4.2 Shape evolution as the sphere sinks

Our model has three dimensionless parameters L, R, h which we need to estimate to perform calculations in the range of values encountered in the experiments. These parameters depend on two dimensional parameters Cw and $\sqrt{Cw/\rho g}$. To estimate them, we approximate C by the storage modulus $G' \simeq 30$ Pa measured in rheology tests in the range of strain rates relevant to the experiment [18]. The thickness of stress boundary layers observed in birefringence experiments is roughly $w \simeq 1$ mm [18]. The density of the
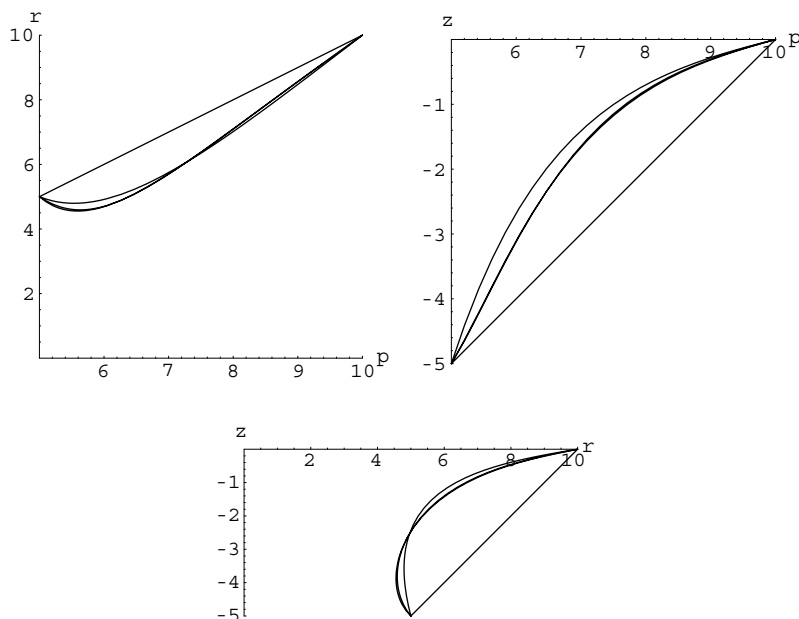
FIGURE 6. Examples of successive iterations in the solution of the system of differential equations, showing the rapid convergence of the functions $r(p)$, $z(p)$ and $r(z)$ from an initially linear approximation.

fluid being close to that of water ($\rho \simeq 1$ g cm^{-3}), the tension scale is $Cw \simeq 0.03$ N m^{-1} = 30 dynes cm^{-1} and the length scale is $\sqrt{Cw/\rho g} \simeq 1.7$ mm. Note that the tension and length scales are close to surface tension and capillary length in most fluids, however the problem is essentially different because of the elastic nature of the membrane: if the deformations are large, the actual tension can be orders of magnitude higher than Cw, according to (3.18) and (3.19). In the experiment, the radii and depth of the sphere for which the phenomenon occurred was on the order of a centimeter, and the half-size of the container was two to three times bigger. Thus, most of the calculations presented below were performed for $L = 10$, R between 2 and 5, and h ranging from 0 to −10. When including the effect of surface tension, we chose $\sigma = 1$ in the dimensionless equations, since Cw is comparable to common values of surface tension.

In our numerical study, the sinking of the sphere is represented by increasing values of the depth h while R and L are kept constant. The equilibrium shape of the membrane depends sensitively on h, as shown by the representative examples in Figure 7. As the magnitude of h increases, the shape of the interface develops a narrow waist, with a minimum radius R_h which decreases as h becomes deeper.

In addition to finding the surface shape, we obtain the evolution of the tension profiles along the surface with h, as shown in Figure 8 as well as the local extension ratios (Figure 9) for the same sequence of deformations in Figure 7. The tension T_1 exhibits a maximum value, which increases as the sphere sinks, and is located at the same level as the narrow waist. The azimuthal tension T_2 behaves in an opposed manner, decreasing its value in the neighborhood of the waist. As these calculations show, for a given
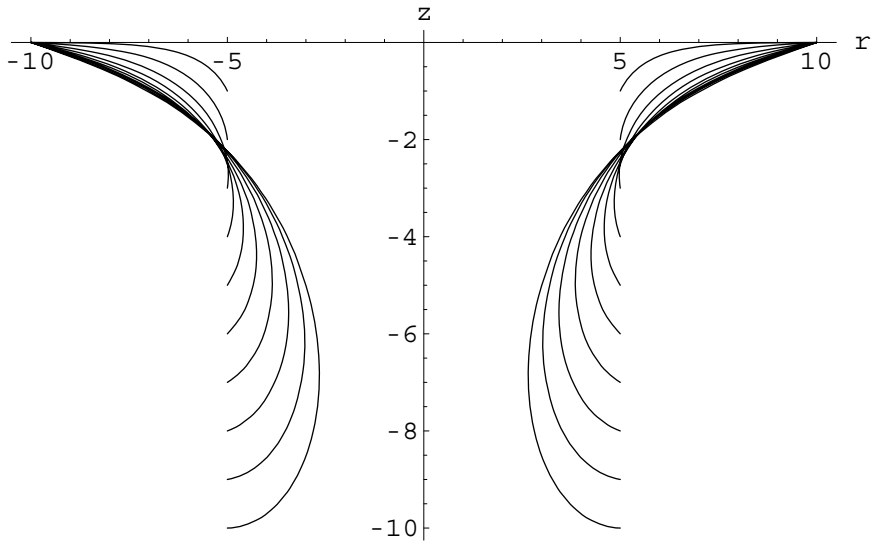
FIGURE 7. Shape evolution of a purely elastic membrane ($\sigma = 0$) for $R = 5$ and $L = 10$, as the depth h ranges from -1 to -10.
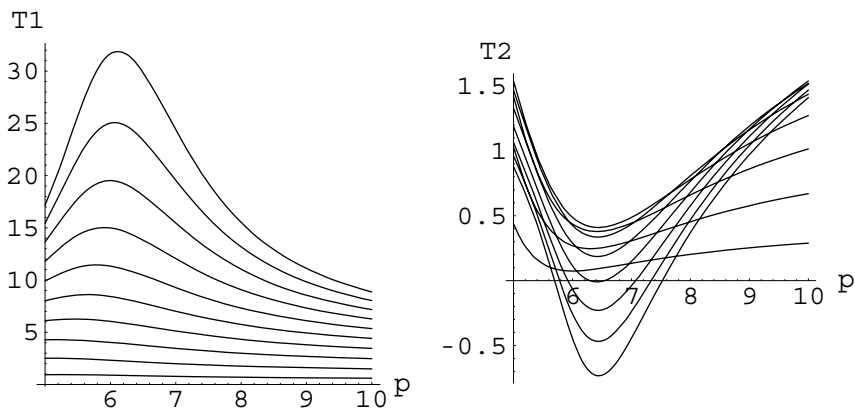

FIGURE 8. Tensions T_1 (meridional) and T_2 (azimuthal), for $R = 5$, $L = 10$, and h from -1 to -10. Note that T_2 becomes negative in a range of p for $h \leqslant -7$.

set of parameters, T_2 can indeed become negative. In other words, the coupled finite elasticity/force balance problem has a solution with a negative azimuthal surface stress; this acts like a negative surface tension and drives the folding instability.

A visual representation of the numerically calculated shape of the membrane as it would appear in 3D is shown in Figure 10, which also depicts the value of the tension T_2 in green and red (see the caption). These images indicate that the membrane becomes unstable once it has been sufficiently stretched, and that the folding instability, driven by the compressive stress ($T_2 < 0$) occurs at the waist of the shape. These aspects agree fully with the experimental observations, and our earlier modeling assumptions [18].
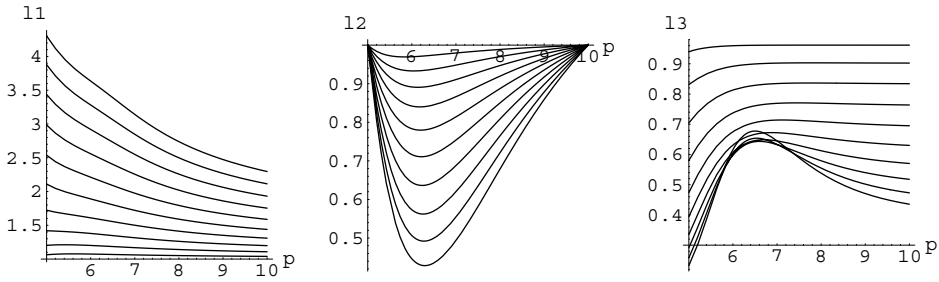
FIGURE 9. Extension ratios λ_1, λ_2, λ_3 ($R = 5$, $L = 10$, for h from 0 to -10).
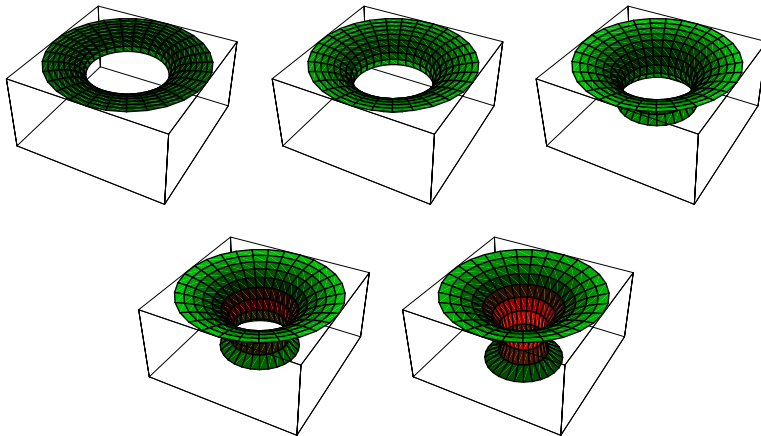
FIGURE 10. Spatial rendering of the calculated membrane shape and tension T_2 at various depths, for $R = 5$ and $L = 10$. From left to right the images correspond to $h = -2, -4, -6, -8$ and -10). The color indicates the sign of the tension T_2, with shades of green representing positive values, while negative values are represented by red.

To explore the parameter dependence of the folding instability, we performed many numerical simulations with different geometric parameters R and h (at fixed $L = 10$), and looked for the appearance of negative tension T_2. To treat the presence of both elasticity and surface tension, as is the case in the experiment, we explicitly separate the two in the force balance equation (3.20):

$$(T_1 + \sigma)\frac{r''z' - r'z''}{(z'^2 + r'^2)^{3/2}} - (T_2 + \sigma)\frac{1}{r(1 + r'^2/z'^2)^{1/2}} + z = 0. \tag{4.1}$$

Note that σ will cancel in (3.21). We performed calculations with nondimensional surface tension $\sigma = 1$ to investigate this effect of surface tension superimposed on elastic tension. This surface tension will in principle counteract the effect of a negative hoop stress. However, the obtained shapes are not significantly different from the purely elastic case, as shown in Figure 11. This is because the elastic force is essentially governed by $T_1 \kappa_1$. Since the deformations are large ($T_1 \gg 1$), the added surface tension is negligible. However, since
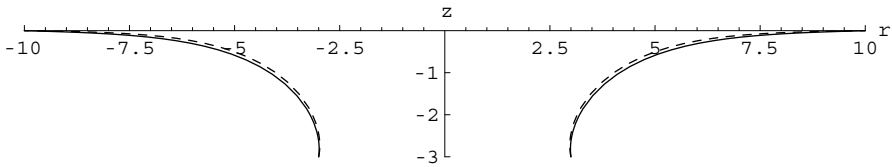
FIGURE 11. Shape of the membrane for $L = 10$, $R = 3$, $h = -3$ with and without surface tension
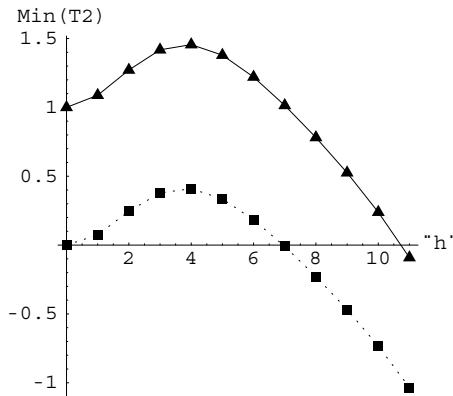(dashed: $\sigma = 0$, solid: $\sigma = 1$).

FIGURE 12. Minimum of the hoop stress T_2 in the membrane for $L = 10$, $R = 3$ and h ranging
from 0 to -11 with and without surface tension (■: $\sigma = 0$, ▲: $\sigma = 1$).

T_2 is generally small, adding surface tension can significantly shift the stability threshold
where T_2 becomes negative: a larger deformation (or equivalently a larger depth h) is
then required to reach the instability condition $T_2 < 0$, as shown in Figure 12.

For $L = 10$, we computed solutions in the (R, h) parameter space to find the stability
condition. Figure 13 shows the corresponding stability diagram. The plane (R, h) is divided
into and upper-right region where $T_2 > 0$ and the membrane is stable to axisymmetric
disturbances, and a lower-left region where $T_2 < 0$, and the folding instability is expected.

The position of the unstable region, below the marginal curve, is consistent with
experimental observations indicating that the instability is triggered only when the sphere
is sufficiently deep.

4.3 Influence of the outer size L

In classical problems of static interfaces, gravity dominates if the overall dimensions of
the system are large compared to the capillary length. For instance, a drop of water
deposited on a horizontal surface is approximately a spherical cap when its size is smaller
than the capillary length $l_c = \sqrt{\sigma/\rho g}$, whereas a large volume turns into a mostly flat
puddle, curved only near the contact line with a radius of curvature of order l_c, and a
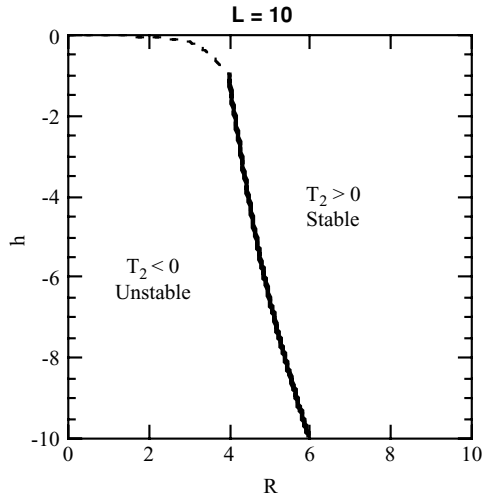thickness of the same order [26].

FIGURE 13. Stability diagram in the (R, h) plane for the membrane, based on the sign of T_2 for a purely elastic membrane ($\sigma = 0$).
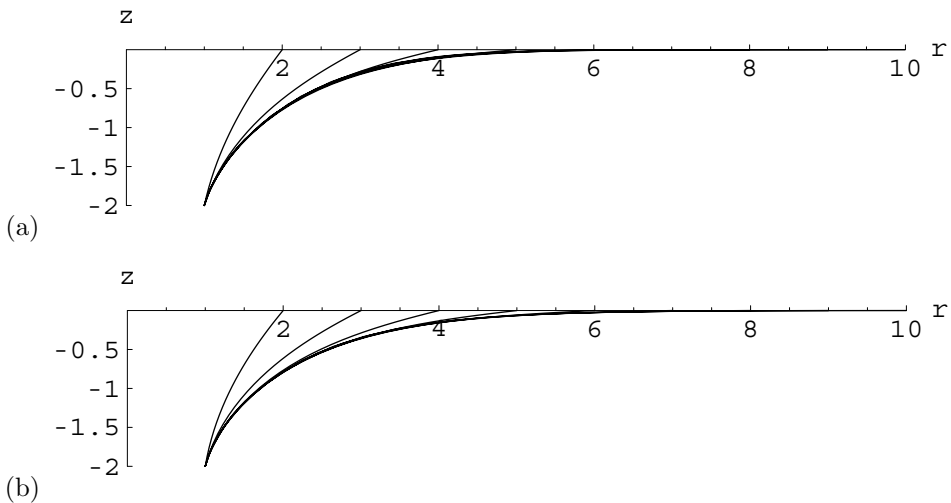

FIGURE 14. Evolution of the membrane shape as L increases from 2 to 10, for fixed $R = 1$ and $h = -2$. (a) $\sigma = 0$ (purely elastic membrane); (b) $\sigma = 1$ (with surface tension).

With an elastic membrane, the same conclusions cannot be drawn as directly, because the tension is not constant. The question of the influence of the lateral dimension of the system L is nevertheless an interesting one: how does the size of the fluid container influence the interface shape around the sinking sphere?

A series of interface shapes were calculated for fixed values of R and h and increasing L, for a purely elastic membrane ($\sigma = 0$), as shown in Figure 14(a), and a membrane with elasticity and surface tension ($\sigma = 1$), as shown in Figure 14(b). The results reveal that
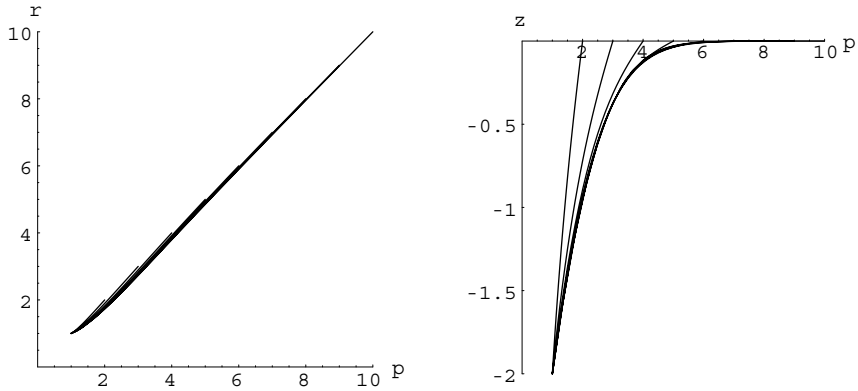
FIGURE 15. Graph of $r(p)$ and $z(p)$ for $R = 1$ and $h = -2$, showing the convergence to an asymptotic solution with increasing L. No surface tension ($\sigma = 0$).
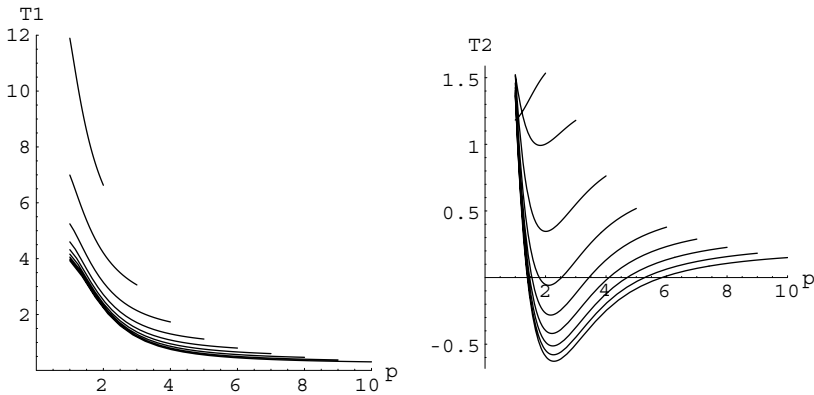

FIGURE 16. Graph of $T_1(p)$ and $T_2(p)$ for $R = 1$ and $h = -2$, showing the convergence to an asymptotic solution with increasing L. No surface tension ($\sigma = 0$).

the membrane shape approaches an asymptotic profile as $L \to \infty$. It converges rapidly to the asymptotic solution as soon as L is greater than the size of the hole (R and h). In other words, if the fluid container is sufficiently large, the interface shape is independent of the overall size. Note that the shape of the membrane is very similar in both cases. This convergence is also clear in Figures 15 and 16.

Intuitively, this is surprising since as L increases the average deformation decreases and this should affect both the tensions and the shape of the membrane. However this can be understood from the following qualitative argument: on average, the pressure term is $h/2$ and does not depend on L. Let us assume that $T_1 \kappa_1$ is the dominant elastic term, which is the case if R is not too small. If the curvature and tension were evenly distributed, an increase in L would result in a decrease of both T_1 and κ_1. Thus the equilibrium can only be achieved by having two regions in the membrane: a curved region where all the deformation and curvature are concentrated, satisfying $T_1 \kappa_1 \simeq h/2$, and a flat unstressed
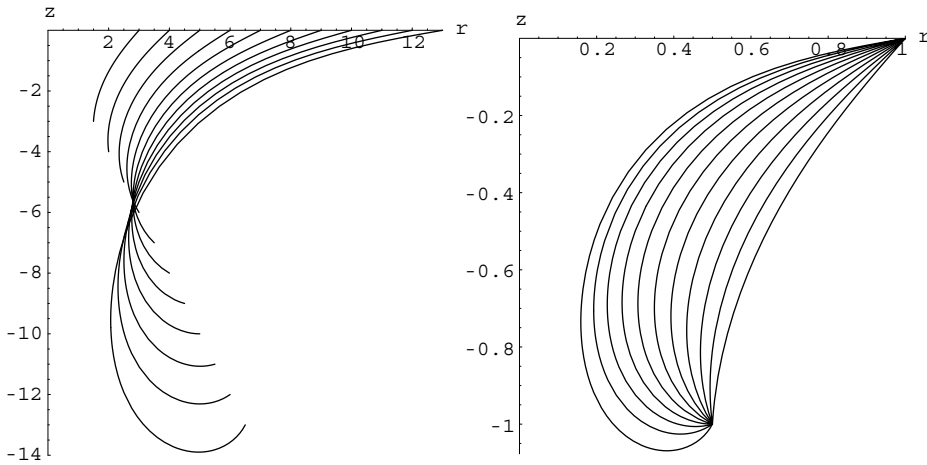
FIGURE 17. (a) Membrane profiles (r, z) for increasing L and fixed ratios $R/L = 0.5$, $h/L = -1$; (b) Rescaled profiles $(r/L, z/L)$.

region, which can be of arbitrary size. The size of the curved region should only depend on h, which sets the order of magnitude of the pressure term.

4.4 Scaling effects: influence of the hydrostatic pressure

Our problem involves a characteristic length $\sqrt{Cw/\rho g}$ used to rescale the equations. By analogy with the regular 'Newtonian' interface case mentioned above, when the size of the system is small compared to $\sqrt{Cw/\rho g}$, elasticity dominates, and the influence of gravity increases with the overall size of the system.

To illustrate this effect, Figure 17(a) shows how the membrane shape is modified when the aspect ratios R/L and h/L are kept constant and L increases. Since all lengths are rescaled with $\sqrt{Cw/\rho g}$, increasing L here is strictly equivalent to keeping the dimensions R, h, L constant and decreasing the value of the characteristic length scale, or increasing the intensity of the gravity term ρg in the dimensional equations. This effect is best seen on the $(r/L, z/L)$ profiles of Figure 17(b). For small L or small gravity, elasticity dominates and the profile is almost straight (the membrane shape is almost a cone). As L increases or as the hydrostatic pressure increases, the curvature increases.

The behaviour of the tensions T_1 and T_2 during this process shows a significant increase (in absolute value) as gravity becomes more and more important (Figure 18). The meridional tension T_1 reaches a maximum which increases with L, as deformation increases, and more importantly, the azimuthal tension T_2 only reaches negative values when L is sufficiently large, or equivalently when the effect of gravity is large enough. This emphasizes the role of the hydrostatic pressure as a necessary condition to reach negative values of T_2, and thus make the buckling instability possible. We provide an analytical calculation in a slightly different geometry (a tube) in Appendix A, which shows that negative hoop stresses cannot be reached without the fluid pressure, no matter how large the deformation is.
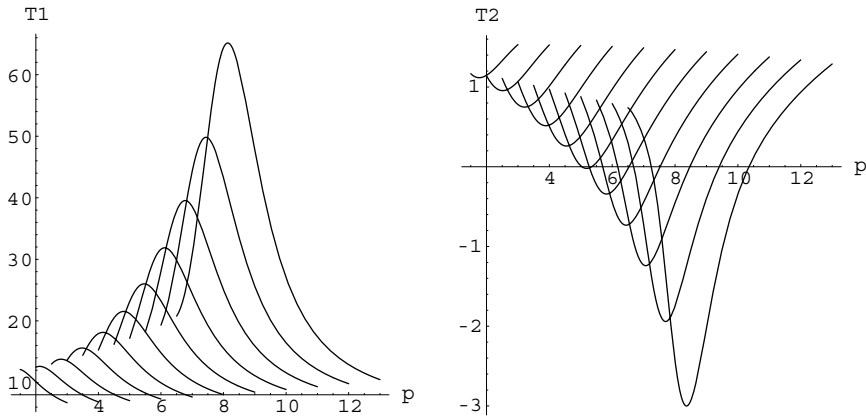
FIGURE 18. Evolution of tension profiles as the overall size of the system increases, with $R/L = 0.5$ and $h/L = -1$.
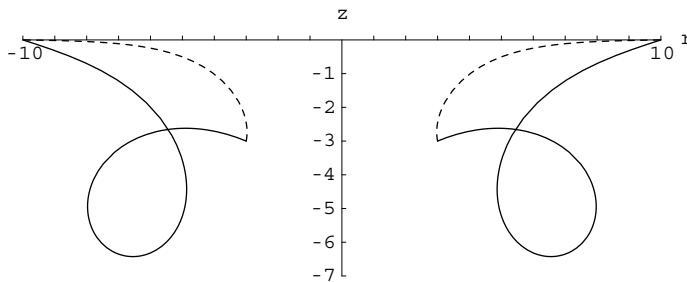

FIGURE 19. Multiple solutions for the shape of the membrane for $L = 10$, $R = 3$, $h = -3$ (dashed: simple solution, solid: "curled" solution).

4.5 Multiplicity of solutions

Our exploration of the parameter space for this problem revealed that multiple solutions to (3.15)–(3.21) exist. Besides the family of funnel-shaped solutions, also seen in the experiments, there exists 'curled' solutions for which the membrane makes loops and intersects itself, as illustrated in Figures 19 and 20. While the hoop stress T_2 never becomes negative in these curled solution (Figure 21), indicating stability to non-axisymmetric disturbances, the values of both T_1 and T_2 are greater than in the non-intersecting solution. This suggests that the total energy of the surface is larger. The curled solutions could either be unstable (if their energy is a maximum) or metastable (if the energy is a local minimum).

From an experimental point of view, these mathematical solutions do not describe what is seen. However, an appealing perspective would be to try to generate such solutions, which could be triggered by somehow forcing the buckling of the unstable "simple" solution in the (r, z) plane, instead of the azimuthal direction. The loop could then correspond to a compressed toroidal air bubble injected into the fluid. Alternatively, if the interior bubble were artificially removed, these solutions might represent cusped stretched
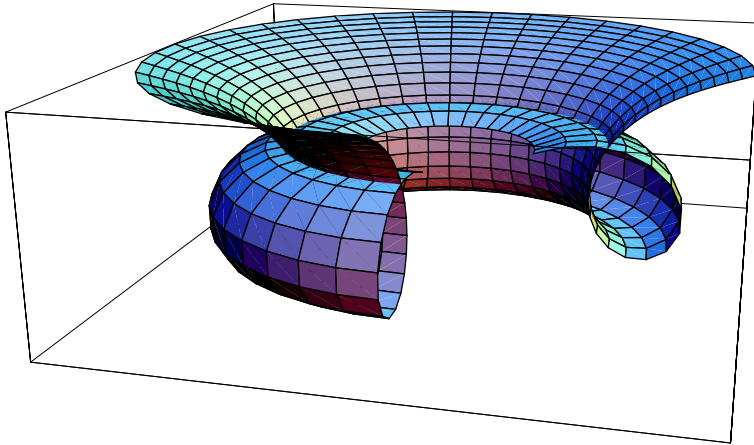
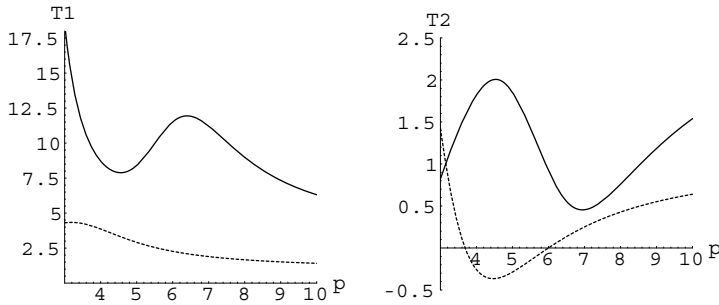FIGURE 20. Tridimensional rendering of the curled solution for $L = 10$, $R = 3$, $h = -3$.

FIGURE 21. Tension profiles along multiple solutions with the same boundary conditions $L = 10$, $R = 3$, $h = -3$ (dashed: simple solution, solid: curled solution).

surfaces, which might be seen if an external forcing were applied such as a periodic shaking; these are purely speculations.

5 Conclusions

In this study we have considered the shape of a stretched viscoelastic interface, driven by the penetration of the fluid surface by a falling sphere. Our finite elasticity membrane model involves the solution of a force balance equation on an unknown axisymmetric shape, coupled to the elastic deformation equations and a neo-Hookean constitutive equation.

One important simplifying assumption in this model is that the volume of the membrane remains constant as the sphere sinks; this should be checked in future experimental work, and any evident dynamics could be included in a revised model. Both force balance and finite elasticity equations may ultimately be treatable within the same variational framework.

The other simplifying assumption is that relaxation occurs over timescales longer than the phenomena we are looking at. Our numerical study of this model shows that negative surface stresses can occur in this geometry, thus driving the folding instability seen experimentally [18]. This may connect to a well-known and not fully solved problem in non-Newtonian fluids, the shape of a rising bubble [14, 16]. In fact, negative surface stresses were also seen in simulations of elastic surface instabilities by Arun Kumar & Graham [1], who suggest this as a mechanism for the asymmetric tail of a rising cusped bubble. As for the dynamics of a viscoelastic free surface and a falling sphere, we have not yet coupled sphere motion or the progressive wetting of its surface to these equations. However, despite its shortcomings, this simple model qualitatively explains the origin of the observed buckling phenomenon.

Acknowledgements

Appendix A Stretching of a neo-Hookean elastic tube

A.1 Problem set up and equations

We consider a purely elastic tube, with no external pressure on the membrane. The reference state is a cylinder of height h_0 and radius R. In the deformed state, the radius of the ends is unchanged, and the length becomes h (Figure A1).

For an elastic tube, the material coordinate p is the z coordinate in the reference state. A material point $M_0(R, p)$ in the reference state maps to $M(r, z)$ in the deformed state. The extension ratios are defined as:

$$\lambda_1 = \sqrt{r'^2 + z'^2} \tag{A 1}$$

$$\lambda_2 = \frac{r}{R} \tag{A 2}$$

$$\lambda_3 = \frac{1}{\lambda_1 \lambda_2}. \tag{A 3}$$

The tensions T_1 and T_2 are defined as previously, and the equations of equilibrium are the same but without the pressure term. Note that because of the absence of pressure, there is no characteristic length in the problem: all dimensions scale out of the equations. Thus the results will only depend on the aspect ratio of the tube, not on the absolute dimensions. All the results given here are for $R = 1$.

The boundary conditions are

$$r(\pm h_0/2) = R \tag{A 4}$$

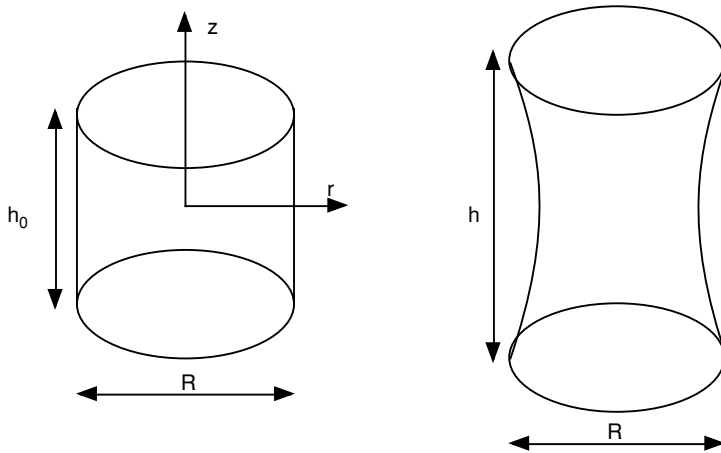$$z(\pm h_0/2) = h/2. \tag{A 5}$$

FIGURE A 1. Notations for the stretched elastic tube model: reference state and stretched state.
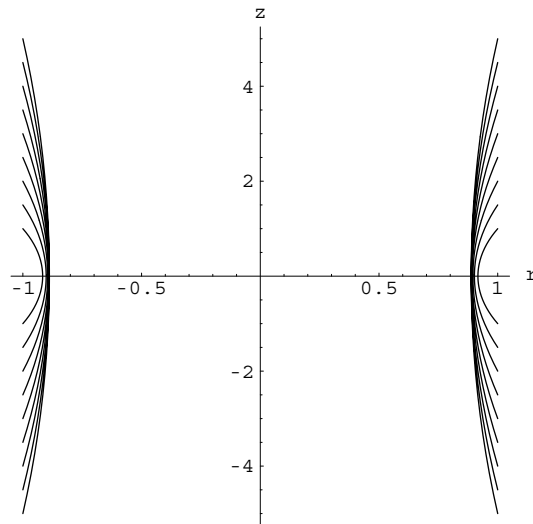

FIGURE A 2. Shape of a stretched elastic tube as h increases from 2 to 10.

We solved the equations using the iterative procedure for a tube with an initial aspect ratio $h_0/R = 1$, with h varying from 2 to 10. A remarkable feature of the obtained shapes is the convergence of the central radius $r(0)$ to a finite value as h increases, as shown in Figure A 2. This is clearly seen on plots of $r(p)$: the function converges to an asymptotic solution (Figure A 3). The function $z(p)$ is almost linear, with a slope increasing proportionally to h.

It is worth noting that although the hoop stress T_2 decreases when h increases, it does not seem to reach negative values, see Figure A 4.
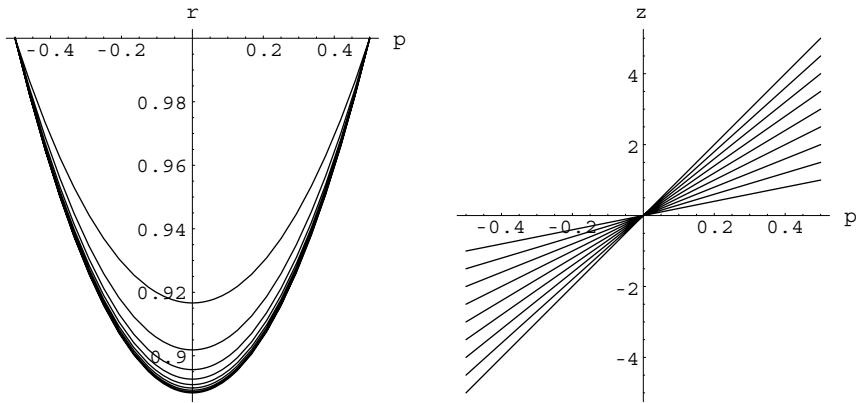
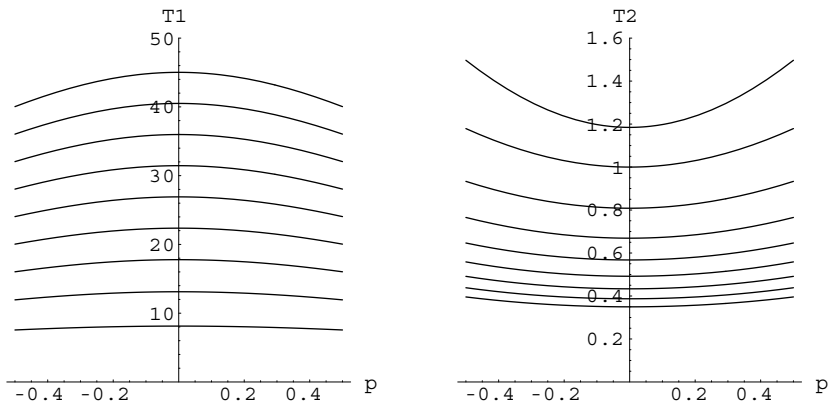FIGURE A 3. $r(p)$ and $z(p)$ as h increases from 2 to 10.

FIGURE A 4. Tensions in a stretched elastic tube with initial length $h_0 = 1$, as the end to end distance h increases from 2 to 10 (T_1 curves are from bottom to top, (T_2 curves are from top to bottom).

A.2 Asymptotic solution

It is possible to calculate analytically the asymptotic solution for $h \to \infty$, after proper simplification of the equations. In the limit $z' \gg r'$ and $\lambda_1 \simeq z' \simeq constant$, the normal force balance reduces to:

$$R^2 r'' - r = 0 \tag{A 6}$$

which has as its solution

$$r(p) = R \frac{\cosh \frac{p}{R}}{\cosh \frac{h_0}{2R}}, \qquad z(p) = \frac{h}{h_0} p \tag{A 7}$$

Note that this solution is a catenoid, however it is not a zero mean curvature catenoid as in the case of the soap film, due to a non uniform and anisotropic tension in the membrane.
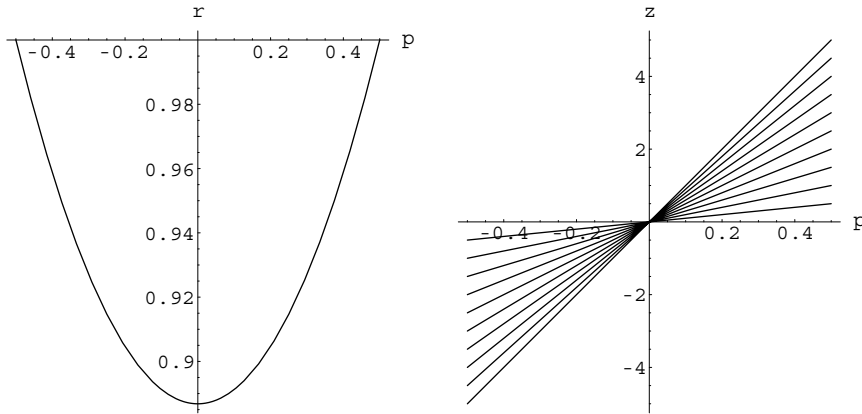
FIGURE A 5. Asymptotic solution for a stretched tube (A 7).

This solution is plotted in Figure A 5, which should be compared to Figure A 3. It can be used to derive the extension ratios λ_1, λ_2, λ_3 and the tensions T_1 and T_2. Of particular interest is the value of T_2 at the waist in this asymptotic regime:

$$T_2(0) = 4 \left(\frac{h_0}{h} \cosh^{-1} \frac{h_0}{2R} - \frac{h_0^3}{h^3} \cosh^3 \frac{h_0}{2R} \right). \tag{A 8}$$

As $h \to \infty$, $T_2(0) \sim 4(h_0/h) \cosh^{-1}(h_0/2R)$, thus the hoop stress is never negative. We conclude from this that a positive pressure difference between the exterior and the interior of the membrane, such as the hydrostatic pressure in our model, is necessary to produce a negative T_2.

The features of the stretched tube described here can be easily observed experimentally by stretching a thin latex tube, such as the finger from a latex glove: when the tube is hollow (the ends are open), it can be stretched with a nearly constant diameter at the waist. If the ends are plugged, a pressure difference builds up between the interior and the exterior as the tube is stretched. This eventually results in a negative hoop stress, and a buckling instability of the tube akin to our folding instability.

References

[1] ARUN KUMAR, K. & GRAHAM, M. D. (2000) Buckling instabilities in models of viscoelastic free surface flows. *J. Non-Newtonian Fluid Mech.* **89**, 337–351.

[2] BIRD, R. B., ARMSTRONG, R. C. & HASSAGER, O. (1987) *Dynamics of Polymeric Liquids*, vol. 1, 2nd ed. Wiley-Interscience.

[3] CHEN, Y.-J. & STEEN, P. H. (1997) Dynamics of inviscid capillary breakup: collapse and pinchoff of a film bridge. *J. Fluid Mech.* **341**, 245–267.

[4] CLANET, C. & QUÉRÉ, D. (2002) Onset of menisci. *J. Fluid Mech.* **460**, 131–149.

[5] COURANT, R. & HILBERT, D. (1962) *Methods of Mathematical Physics*, volume 2. Wiley-Interscience, 1962.

[6] DE GENNES, P. G. (1985) Wetting: Statics and dynamics. *Rev. Mod. Phys.* **57**, 827–863.

[7] DUFFY, B. R. & MOFFATT, H. K. (1995) Flow of a viscous trickle on a slowly varying incline. *Chem. Eng. J.* **60**, 141–146.

[8] ELGSAETER, A., STOKKE, B. T., MIKKELSEN, A. & BRANTON, D. (1986) The molecular basis of erythrocyte shape. *Science*, **234**, 1217–1223.

[9] FOREST, M. G. & WANG, Q. (1990) Change-of-type behavior in viscoelastic free jets. *J. Theor. Comput. Fluid Mech.* **2**, 1–25.

[10] GELFAND, U. M. & FOMIN, S. V. (1963) *Calculus of Variations.* Dover.

[11] GREEN, A. E. & ADKINS, J. E. (1960) *Large Elastic Deformations.* Oxford University Press.

[12] HARLEN, O. G., HINCH, E. J. & RALLISON, J. M. (1992) Birefringent pipes: the steady flow of a dilute polymer solution near a stagnation point. *J. Non-Newtonian Fluid Mech.* **44**, 229–265.

[13] HARLEN, O. G., RALLISON, J. M. & CHILCOTT, M. D. (1990) High-Deborah number flows of dilute polymer solutions. *J. Non-Newtonian Fluid Mech.* **34**(3), 319–349.

[14] HASSAGER, O. (1979) Negative wake behind bubbles in non-Newtonian liquids. *Nature*, **279**, 402–403.

[15] KAMPAS, F. (1998) Iterative solution of highly non-linear equations using Mathematica. *1998 Worldwide Mathematica Conference.*

[16] LIU, Y., LIAO, T. & JOSEPH, D. D. (1995) A two-dimensional cusp at the trailing edge of an air bubble rising in a viscoelastic liquid. *J. Fluid Mech.* **304**, 321–342.

[17] MIDDLEMAN, S. (1995) *Modeling Axisymmetric Flows: Dynamics of films, jets, and drops.* Academic Press.

[18] PODGORSKI, T. & BELMONTE, A. (2002) Surface folds during the penetration of a viscoelastic fluid by a sphere. *J. Fluid Mech.* **460**, 337–348.

[19] RASMUSSEN, H. K. & HASSAGER, O. (1999) Three-dimensional simulations of viscoelastic instability in polymeric filaments. *J. Non-Newtonian Fluid Mech.* **82**, 189–202.

[20] REHAGE, H. & HOFFMANN, H. (1991) Viscoelastic surfactant solutions: model systems for rheological research. *Molecular Phys.* **74**, 933–973.

[21] RENARDY, M. (2000) Wall boundary layers for Maxwell liquids. *Arch. Rational Mech. Anal.* **152**, 93–102.

[22] SEIFERT, U., BERNDL, K. & LIPOWSKY, R. (1991) Shape transformations of vesicles – phase diagram for spontaneous curvature and bilayer coupling models. *Phys. Rev. A*, **44**, 1182–1202.

[23] SMOLKA, L. B. & BELMONTE, A. (2003) Drop pinch-off and filament dynamics of wormlike micellar fluids. *J. Non-Newtonian Fluid Mech.* **115**, 1–25.

[24] SPIEGELBERG, S. H. & MCKINLEY, G. H. (1996) Stress relaxation and elastic decohesion of viscoelastic polymer solutions in extensional flow. *J. Non-Newtonian Fluid Mech.* **67**, 49–76.

[25] STONE, H. A., LIMAT, L., WILSON, S. K., FLESSELLES, J.-M. & PODGORSKI, T. (2002) Corner singularity of a contact line moving on a poorly wetting substrate. *C. R. Acad. Sci. (Paris) IV*, **3**, 103–110.

[26] TAYLOR, G. I. & MICHAEL, D. H. (1973) On making holes in a sheet of fluid. *J. Fluid Mech.* **58**, 625–639.

[27] YAO, M. & MCKINLEY, G. H. (1998) Numerical simulations of extensional deformations of viscoelastic liquid bridges in filament stretching devices. *J. Non-Newtonian Fluid Mech.* **74**, 47–88.

[28] YOUNG, T. (1805) An essay on the cohesion of fluids. *Phil. Trans. R. Soc. Lond.* **95**, 65–87.